ACCSCIENCE PUBLISHING

Journal of Seismic Exploration

ARTICLE

# Microtremor investigation and geological verification of the eastern segment, north margin active fault of Hami Basin, Xinjiang, China

**Xu Song[1,2,3†], Guanghong Ju[4†], and Jun Shen[1,2,3*]**

[1]Institute of Disaster Prevention, Sanhe, Hebei, China

[2]Beijing Disaster Prevention Science and Technology Corporation Limited, Beijing, China

[3]Hebei Key Laboratory of Earthquake Dynamics, Sanhe, Hebei China

[4]Power China Northwest Engineering Corporation Limited, Xi'an, Shaanxi, China

## Abstract

The eastern section of the Northern Margin Fault of the Hami Basin is located in the easternmost part of the active tectonic belt of the Tianshan Mountains, and is an important active fault in the region. Since major projects need to consider avoiding or adopting anti-fracture measures, it is necessary to determine the exact location of the fracture, three-dimensional (3D) orientation, and other anti-fracture-related parameters. To obtain the accurate location and 3D geometric parameters of the rupture, we carried out a systematic study in three typical sites based on remote sensing interpretation and geomorphological survey, and the comprehensive use of microdynamic detection and trench verification. The results show that the fracture section is spreading in east–west direction, with a total length of about 35 km, and is dominated by retrograde movement, which is geomorphologically manifested as a fault steep canyon on the pre-hill flood fan, with the height of steep canyon up to 11–13 m. The microdynamic profiles reveal the deep production of the fracture, with the width of the fracture zone ranging from 60 to 100 m, and the dipping angle ranging from 60° to 70°; and the trench validation reveals that the dipping angle of the faults is slowing down to 35°–45° at the surface, showing a "deep and steep" pattern, and the "deep and steep dipping angle" is also shown. The geometrical structure of the fault is characterized as "deep, steep, and shallow." As an emerging geophysical detection method, the micro-motion detection technique used in the study showed good recognition ability in complex terrain and thick cover conditions, improving the detection accuracy of fracture location. The results of the study not only enrich the understanding of the active features of the Northern Margin Fault of the Hami Basin, but also provide the fault resistance parameters for the evaluation of regional seismic hazard and the selection of sites for major projects, and expand the scope of application of the micro-motion detection method in the study of active faults, providing an important reference for the regional tectonic evolution and seismic resistance of the project.

***Keywords:*** Eastern segment of the Northern Margin Fault of the Hami Basin; Microdynamic detection; Groove; Geometric structure

†*These authors contributed equally to this work.*

***Corresponding author:**
Jun Shen
(shenjun@cidp.edu.cn)

**Citation:** Song X, Ju G, Shen J. Microtremor investigation and geological verification of the eastern segment, north margin active fault of Hami Basin, Xinjiang, China. *J Seismic Explor*. doi: 10.36922/JSE025380073

**Received:** September 18, 2025

**Revised:** November 20, 2025

**Accepted:** November 24, 2025

**Published online:** December 23, 2025

## 1. Introduction

The northern margin fault of the Hami Basin is located at the boundary between the eastern part of the Tianshan Orogenic Belt and the Hami Basin. It is one of the most important active faults that determine the topography and structure of the eastern Tianshan region. This fault is a deep and major fault that cuts through the Moho discontinuity.[1] Located at the easternmost end of the active Tianshan orogenic belt, the area is characterized by the weakest current tectonic activity within the Tianshan Mountains. Its Late Quaternary deformation intensity is markedly lower than that of major faults in the western and central Tianshan regions. In recent years, as research into the tectonic dynamics and neotectonic movements of the eastern Tianshan has deepened, the Northern Margin Fault of the Hami Basin has also become a focal point of investigation.

Existing studies have mainly relied on remote sensing image interpretation and geomorphological survey methods to preliminarily identify the macroscale distribution characteristics of the northern margin fault of the Hami Basin, and analyzed its activity by combining the Quaternary stratigraphic features and gully displacement phenomena.[2] The northern margin fault of the Hami Basin extends for around 300 km along the southern foothills of the Baryn and Halik mountains. The segment along the southern foothills of the Baryn Mountains is usually referred to as the western segment, and the segment along the southern foothills of the Halik Mountains as the eastern segment (Figure 1). Based on the geometric distribution characteristics of the fractures, the western section is divided into the Dewaoli segment, Xishan segment, and Zhongyingtai segment; the eastern section is divided into the Shichengzi segment, Shangmiyang-Bamudun segment, and Dongtaizi segment. Research on the Northern Margin Fault of the Hami Basin has largely focused on the western segment between Dewaoli and Zhongyingtai. The Dewaili segment extends approximately 50 km from west of Liushugou Village eastward through Dewaili Township to Sidaogou. Using cosmogenic nuclide dating, the vertical slip rate of this fault segment was determined to be 0.10–0.18 mm/year.[2] The Xishan segment, approximately 24 km long, extends eastward from Akta to Xishan Township. High-precision digital elevation model data acquired through unmanned aerial vehicles was combined with chronological sample test results to calculate the sliding rates for Xishan, ranging from 0.06 to 0.08 mm/year.[3] The Zhongyingtai segment spans approximately 25 km, extending from Hulugou through Xiwudeke to the Nanshankou area. Thermoluminescence dating indicates an average vertical slip rate of 0.31 ± 0.03 mm/year for this segment.[4] However, due to inherent limitations of thermoluminescence dating, the results for landform surface ages may not be precise. The Shichengzi segment extends eastward from Shichengzi to the Yushugou area, with a surface trace length of approximately 10 km; the Shangmiyang segment extends from the Shangmiyang tributary to the Bamudun area, approximately 35 km long; the Dongtaizi segment extends eastward from Bamudun through Wulaitai to the area east of Tianshengquan, with a surface trace length of approximately 25 km. Due to the fault's considerable length, slip rates along its strike exhibit spatial and temporal variations. Consequently, the slip rate at any single point cannot fully represent the activity intensity of the entire fault. However, from a spatial distribution perspective, the slip rates of the Dewaili and Zhongyingtai segments are largely consistent, while the Xishan segment exhibits a slightly lower slip rate. Temporally, the slip rate remained relatively stable from the late Middle Pleistocene to the mid-Late Pleistocene.

The eastern portion of the northern margin fault in the Hami Basin has been less extensively studied compared to the western segment. No dedicated research has been conducted into its spatial distribution, precise location, or most recent period of activity. Investigations into active faults require not only the collection of macroscopic data on the geometric and kinematic characteristics of the fault to assess seismic hazard, but also the determination of its precise location and three-dimensional (3D) orientation. This is essential for engineering projects that require active faults to be avoided or anti-fault measures to be implemented (Figure 2). The eastern segment of the northern margin fault primarily develops within a foothill zone consisting of bedrock, landslide deposits, and coarse-grained slope-alluvial sediments. Fault dislocation landforms and geological outcrops are not distinctly evident. Research methodologies should therefore incorporate geophysical techniques, remote sensing interpretation, and field geological and morphological surveys. Current geophysical methods for active fault studies primarily encompass seismic, electromagnetic, and microgravity techniques.[5-8] This study investigates the 3D orientation of the northern margin fault in the Hami Basin by integrating microtremor detection with geological and geomorphological surveys.

Microtremor survey method uses faint vibrations on the Earth's surface that are not caused by seismic activity for exploration purposes.[9,10] This technique is crucial for identifying shallow geological structures and active faults. This technique uses faint surface vibration signals as natural seismic sources to reflect the velocity structure of strata

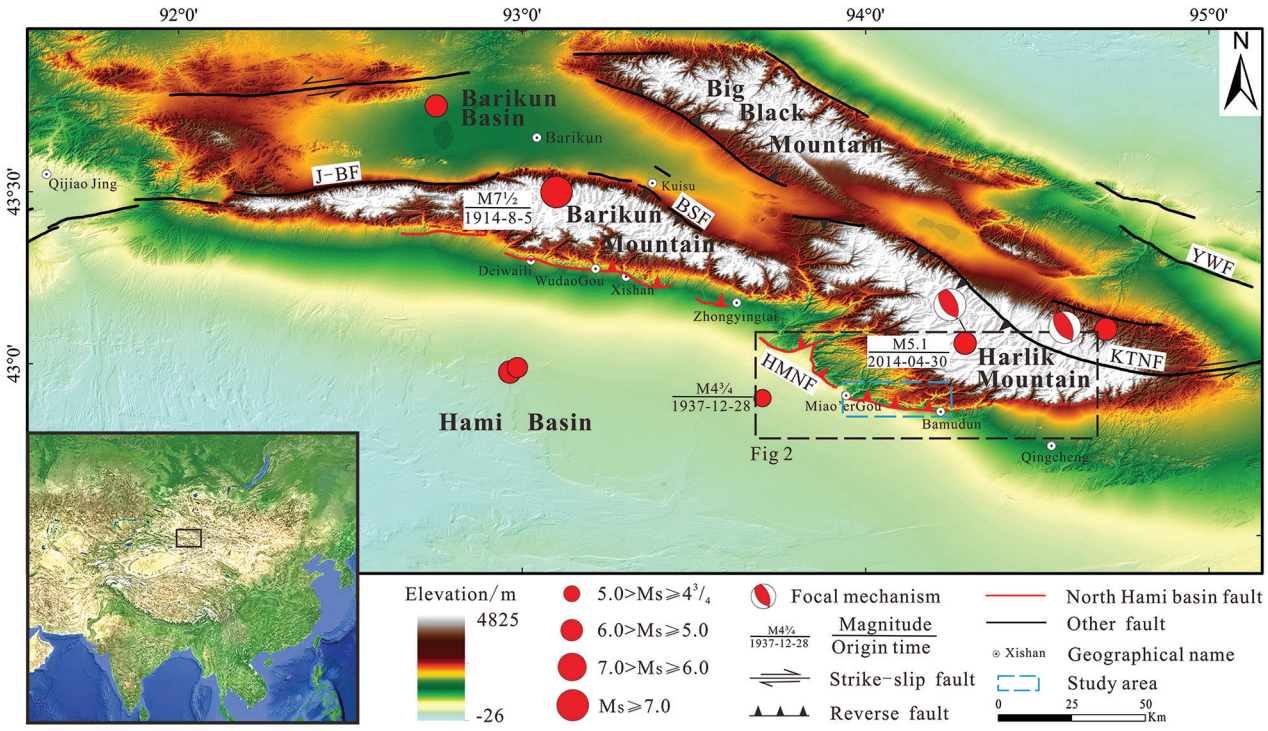


**Figure 1.** Regional fault distribution map
Abbreviations: HMNF: Northern Margin Fault of the Hami Basin; NKTF: Harlik Mountains North Margin Fault; YWF: Yiwu Basin South Margin Fault.

and site characteristics effectively. Compared to traditional artificial-source methods, microdynamic detection offers advantages such as strong interference resistance, high operational efficiency, and terrain adaptability.

In recent years, the microtremor survey method has been increasingly widely used in active fault research. Early studies revealed the subsurface velocity structure in the Kanto Plain via the spatial autocorrelation (SPAC) method[11] and confirmed the non-linear relationship between the subsurface shear wave velocity structure and dispersion curves using the divergent genetic algorithm.[12] With the development of technology, the applicability of this method has been further expanded: the S-wave velocity structure within a depth range of 100 m has been successfully obtained using microtremor arrays,[13] and background noise imaging with dense arrays has also verified the feasibility of inverting the broadband Rayleigh wave phase velocity.[14] At the application level, microtremor surveys have been effectively applied to multiple aspects, such as the precise location of concealed faults,[15] subsurface geological stratification, and concealed structure detection,[16-18] providing important technical support for active fault research.

In this study, we used microtremor detection methods combined with remote sensing, geological and topographical surveys, and trenching techniques to determine the exact location and 3D orientation of the eastern part of the northern margin fault in the Hami Basin, yielding relevant parameters for the engineering avoidance of active faults and the engineering resistance to faulting. This research also addresses the lack of studies on this fault segment and improves our understanding of the active characteristics and deformation mechanisms at the easternmost tip of the Eastern Tianshan Mountains. Furthermore, it contributes to the body of case studies on microtremor detection in active fault research, thereby promoting the wider application of this method. In addition, through this study, we explore the methods for detecting active faults beneath coarse-grained debris flow deposits.

## 2. Geological setting

The Tianshan Orogenic Belt is a typical reactivated intra-continental orogenic belt within the Eurasian continent[19] and is one of the region's largest young mountain systems. Its tectonic evolutionary history can be traced back to the Late Palaeozoic era. It subsequently underwent renewed compression and uplift during the Cenozoic era due to the long-range effects of plate collision, thereby forming a prototypical intra-continental reactivated orogenic belt.[20-24] North-south shortening deformation is regulated

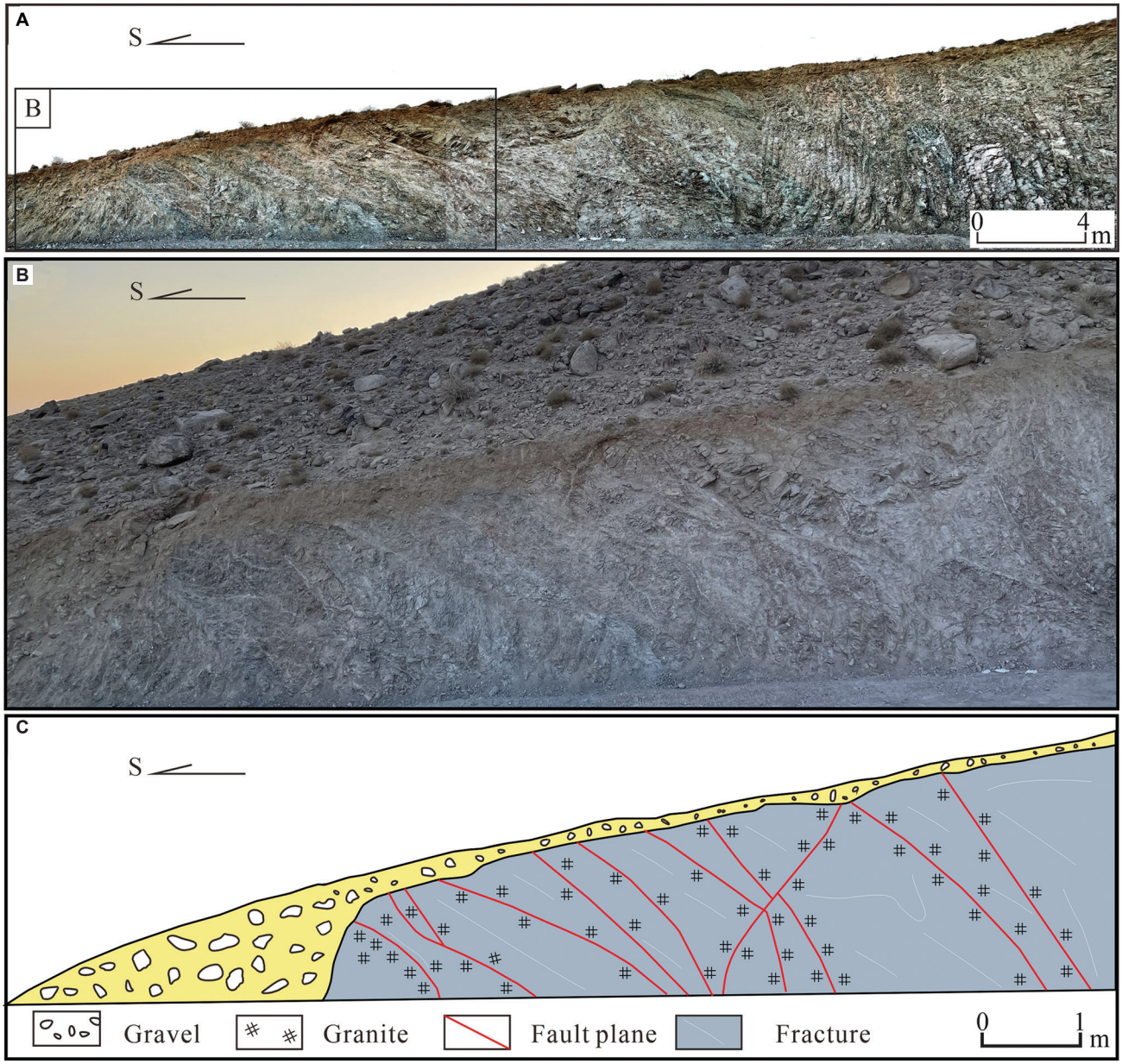


**Figure 2.** Photographs and structural profile of the fault outcrop exposed at the adit portal. (A). Overview photograph of the fault outcrop, looking toward the west; (B) Close-up view of the main fracture zone, looking toward the west; (C) Interpretive cross-section illustrating the geometry of the main fault.

and accommodated by thrust faults in the foreland and large-to-medium strike-slip faults within the mountain basins.[25,26] The eastern and western Tianshan exhibit distinct tectonic patterns and activity intensities; the eastern Tianshan demonstrates a significantly lower crustal shortening rate than the western Tianshan.[27-29] Previous studies indicate that active faults in the eastern Tianshan region exhibit a gradual decrease in slip rate from west to east.[30] Furthermore, the easternmost Halik Mountains region adjoins the Altai uplift zone to the north and the Gobi–Altai tectonic transition zone to the east. This region is situated at the junction of the active Tianshan tectonic zone and the Western Mongolian tectonic activity zone.[31-33]

The northern margin fault of the Hami Basin, located in the Eastern Tianshan region, is an important part of the Tianshan orogenic belt. The collision and ongoing convergence of the Indo-Eurasian plates have had a pronounced effect on it, forming a typical reactivated intra-continental orogenic belt. As a key active fault in the eastern part of the Eastern Tianshan region, it exerts significant control over the geological structural pattern of the northern margin of the Hami Basin. The region features

multi-tiered foreland alluvial fans, with extensive alluvial gravel surfaces interbedded with coarse landslide debris and minor aeolian loess deposits. The underlying bedrock is primarily granite or Neogene strata. The spaces between adjacent alluvial fans are predominantly filled with coarse landslide debris or bedrock.

The northern margin fault of the Hami Basin runs from the Hami Basin to the Baryn and Kalik mountains. In terms of geotectonics, it forms a boundary fault that separates the ancient North Tianshan island arc belt from the Hami terrane.[21] The fault generally trends from northwest to northeast, extending for around 300 km. Its western extension potentially connects with the Jianquanzi–Barkol Fault, while its eastern terminus may be linked to the left-lateral strike-slip fault system of the Gobi Tianshan. The northern margin fault of the Hami Basin is clearly visible in satellite imagery as a series of linear features and is evident topographically as a series of discontinuous fault scarps on the alluvial fan at the foothills (Figure 3). Fault activity shows pronounced NE-SW convergence,[34] with post-Late Quaternary activity controlling the coupling between the Hami Basin and the Eastern Tianshan Mountains. However, seismic activity along the northern margin fault remains relatively low. Instrumental records indicate comparatively weak tectonic movement, slow energy accumulation, and infrequent occurrence of minor seismic events.[35]

## 3. Methodology

This study focuses on the eastern segment of the northern margin fault in the Hami Basin. Using a comprehensive approach that incorporates microtremor detection techniques and trench investigations, it employed remote sensing image interpretation and field geological and geomorphological surveys to systematically examine the fault's planar distribution characteristics and profile features.

### 3.1. Integrated remote sensing interpretation and field investigation

Accurately determining the spatial location of the fault is fundamental to identifying and analyzing its activity. Remote sensing image interpretation is an important means of understanding the distribution of faults and provides key control for subsequent field surveys and geophysical exploration.

This paper is based on the AuVue interactive map platform, and various high-resolution remote sensing image data were collected and organized, including data from the Four Dimensions Earth and Jilin-1 satellites. By combining 2D planar images and 3D visualization models, the area around the temple gully and the Bayugundu River was remotely interpreted, and the main fractures in the study area were identified and extracted (Figure 4).

The study area lies between the Yagudun and Miaogou rivers, spanning a total length of approximately 35 km. The two rivers formed three-tiered terraces on the eastern and western sides of the study area, respectively. Multiple alluvial fans of varying scales and distinct morphologies lie between these two rivers. Comparing with the research results in adjacent areas, for example, the existing dating results of the abandonment age of alluvial fans in Dewaili and Xishan areas show that the alluvial fans within the study area can be classified into three main stages.[4] They formed sequentially in the Middle or Early Late Pleistocene (Fan1), the Late Pleistocene (Fan2), and the Holocene (Fan3). Fault scarps developed intermittently on Fan2 and Fan3, whereas they are less clearly defined on Fan1.

To the west of the mouth of the Yagudun River and to the east of the mouth of the Miaogou River, the foreland area exhibits distinct fault-block topography, characterized by escarpments that are distributed intermittently across the Late Pleistocene alluvial-fluvial fan. Field investigations and tracing along the fault strike revealed distinct escarpments

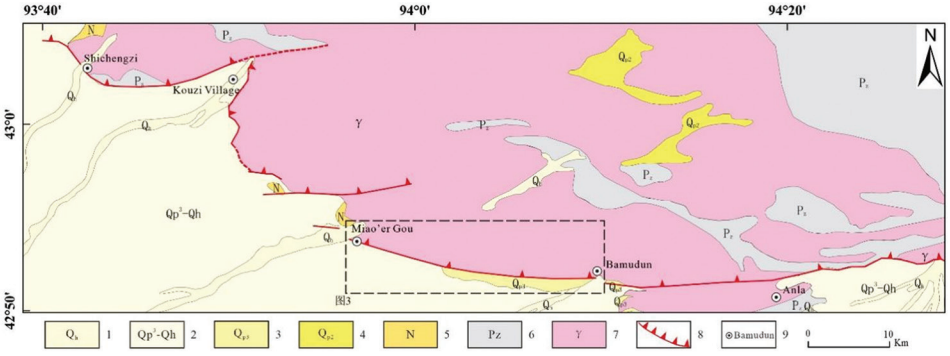


**Figure 3.** Fracture map of the northern margin of the Hami Basin. (1) Holocene Series; (2) Upper Pleistocene–Holocene Series; (3) Upper Pleistocene Series; (4) Middle Pleistocene Series; (5) Neogene System; (6) Paleozoic Erathem; (7) Granite; (8) Northern Margin Fault of Hami Basin; (9) Place name.

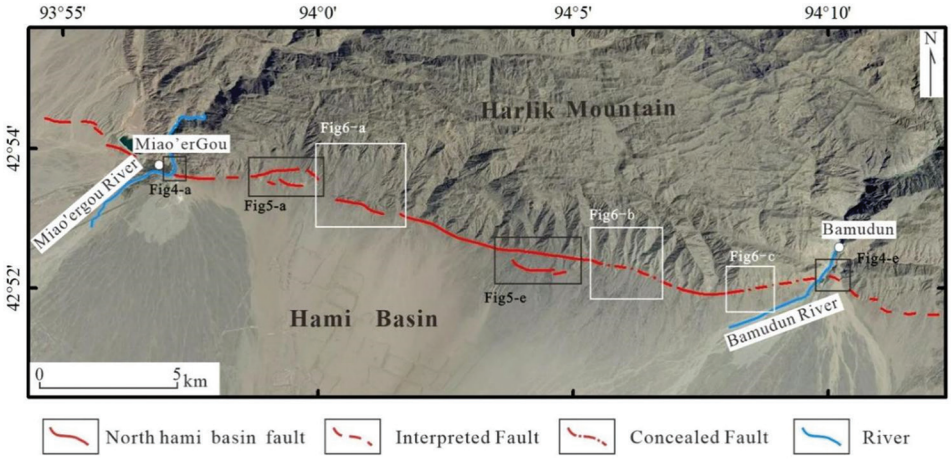


**Figure 4.** Distribution map of faults in the research area

on the foreland alluvial fan. The higher T3 terrace has escarpments reaching heights of up to 11 m, while the T2 terrace has escarpments of 1–3 m. No significant faulting deformation is evident on the T1 terrace.

Figure 5A shows satellite image of the left bank of the Miaogou River. Along the left bank, on Terrace T3, a series of distinct fault scarps is clearly visible. These scarps exhibit pronounced topographic boundaries in the image, indicating significant vertical displacement. In contrast, no pronounced faulting was observed on the river terraces, likely due to their incomplete development and human alterations. Figure 5B shows a photograph taken in the field of the fault at the leading edge of the foreland fan. The image reveals a distinct fault scarp on Terrace T3 with an approximate height of 12 m.

Moreover, a fault section has been exposed by an artificial road cutting along the lateral margin of the alluvial fan at the mouth of Miaogou Gully. This fault exhibits thrusting characteristics, with the exposed section showing brick-red Neogene mudstone being thrust northwards onto gravelly deposits (Figure 5C). Figure 5D shows the geological cross-section, with the fault plane marked by a red line at an inclination of approximately 40°. There is a significant lithological contrast on either side of the fault: the hanging wall consists of granite overlain by fluvial-alluvial gravel, while the footwall comprises fluvial-alluvial gravel.

Figure 5E shows the T3 terrace on the left bank of the Yagidun River. This terrace exhibits distinct fault characteristics that correspond to those of the Miaogou River terrace (Figure 5A). Figure 5F depicts the eastern bank of the Bayudun River. A distinct fault scarp, measuring around 13 m in height, can be seen on the river terrace along the eastern bank at the river's outlet. This further corroborates the presence of active tectonic features on the river terraces within the study area.

Figure 6A is located 2.3 km east of Miaogou and preserves remnants of the Fan3 alluvial fan. Faulting activity in this area has created a discontinuous fault-block topography that appears as steep fault scarps with exposed red strata on remote sensing image (Figure 6A and B). These steep escarpments are adjacent to the alluvial fan deposits at the foot of the mountains, exhibiting well-defined morphology. This further confirms the active nature of the fault since the Late Quaternary period (Figure 6B). Figure 6C depicts an active fault outcrop at the location shown in Figure 6A, while Figure 6D presents the corresponding cross-section. The cross-section shows that the hanging wall of the fault consists of red sandstone and mudstone from the Neogene, which is overlain by a layer of coarse cobbles and gravel. Due to fault displacement, the red Neogene mudstone has undergone tensile deformation, and no red strata are visible beneath the gravel layer on the footwall.

Figure 6E shows a series of steep, discontinuous fault scarps distributed across the Fan2 alluvial fan, approximately 2 km west of the Yagidun River. The cumulative height of these scarps is up to 11 m (Figure 6F).

A comprehensive interpretation of remote sensing image and field survey findings reveals that a series of steep escarpments has developed extensively across the foreland slopes, from the Miaogou River to the Bamudun River. These escarpments are predominantly located at the edges of alluvial fans or at the interface between bedrock and loose deposits. However, as the morphology of some escarpments may be influenced by non-tectonic factors such as differential erosion, uneven deposition, or landslide accumulation, surface morphology alone is insufficient to definitively determine whether they are the result of fault displacement. Therefore, to clarify the presence of faults at the locations of these escarpments, verification through microtremor and trenching investigations is required. This

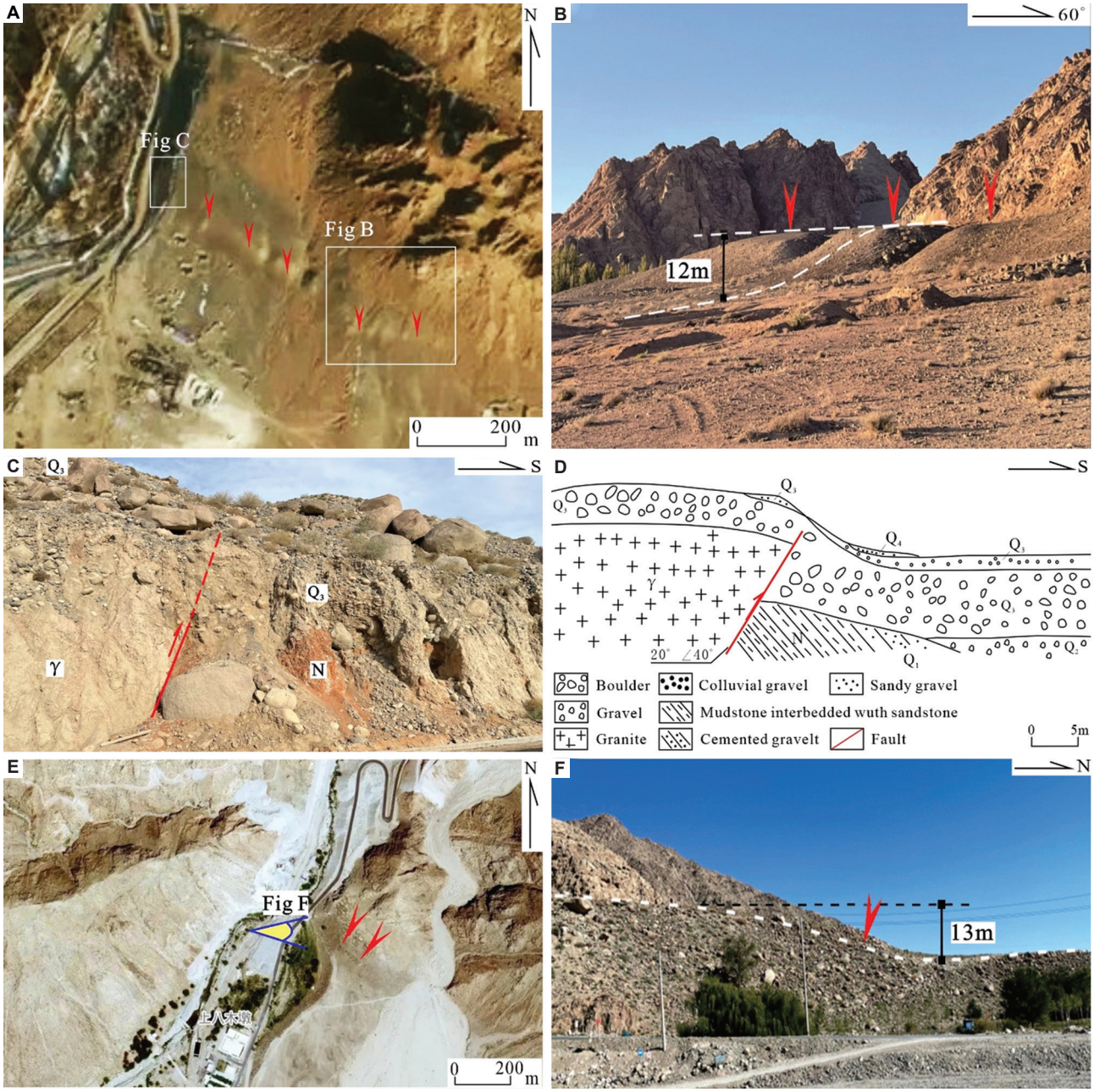


**Figure 5.** A faulted steeple on a floodplain fan. (A) Remote sensing image showing fault scarp on the left bank of Miaoergou River; (B) Photograph of the fault scarp on the left bank of Miaoergou River. (C) Fault outcrop in the piedmont alluvial fan at the estuary of Miaoergou River; (D) Profile of the fault outcrop in the piedmont alluvial fan at the estuary of Miaoergou River; (E) Image of the fault scarp on the T3 terrace of the left bank of the Bamudun River; (F) Photograph of the fault scarp on the T3 terrace of the left bank of the Bamudun River.

approach also provides more compelling evidence for the precise location and 3D orientation of the fractures.

### 3.2. Microtremor survey

To determine the exact location of the fault more precisely, ascertain the width of the fault zone, and reveal its downward extension and profile characteristics, we deployed microtremor survey lines at three locations spanning the steep escarpments of the Xinxing, Xinxing East, and Hongxing pumped-storage hydropower stations (Figure 7). The aim is to verify the existence of the fault and, in conjunction with geological and topographical surveys, determine its 3D orientation.

Given the actual conditions of the study area, the GN309 microtremor detection system developed by Hefei Guowei Electronics Co., Ltd. was employed for microtremor data

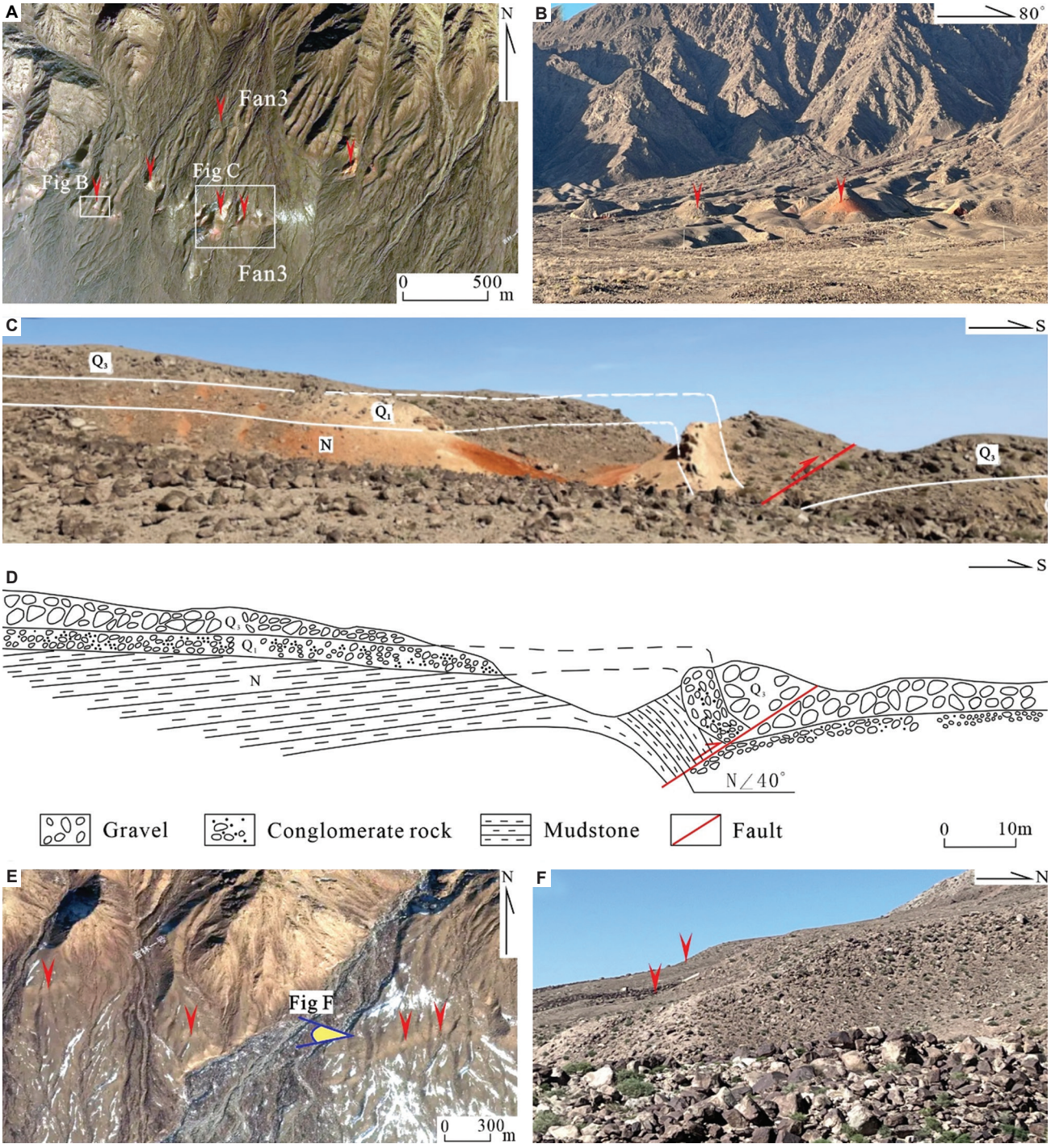


**Figure 6.** Images of a faulted steeple on a floodplain fan. (A). Remote sensing image of the area 2.3 km east of Miaoergou; (B) Photograph of the fault scarp 2.3 km east of Miaoergou; (C) Fault outcrop, west of the Lower Reservoir of Xinxing Pumped Storage Power Station; (D) Profile of the fault outcrop, west of the Lower Reservoir of Xinxing Pumped Storage Power Station; (E) Image of the fault scarp, situated at 2 km west of Bamudun River; (F) Photograph of the fault scarp, situated at 2 km west of Bamudun River.

acquisition. Three microtremor survey lines were deployed on-site. To accurately infer fault locations, all three lines traversed trenches: MTS-a (1.6 km), MTS-b (1 km), and MTS-c (1 km). Station spacing was 10 m, with a sampling rate of 2 ms and a sampling duration of 30 min. All three lines employed a straight-line regular array layout, utilizing an active-source excitation with reverse-phase observation for data acquisition. During data processing, surface wave

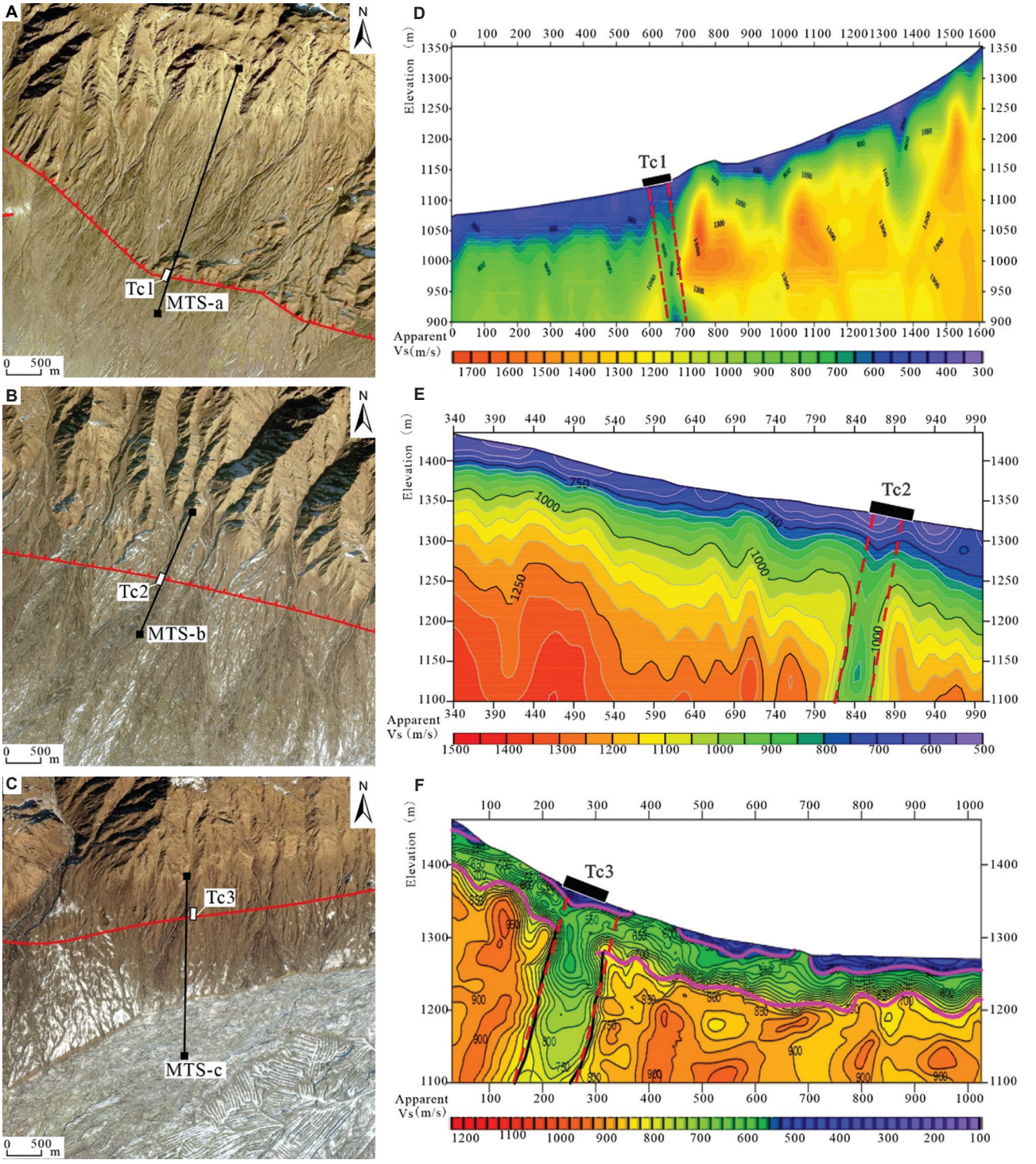


**Figure 7.** Analysis diagram of micromotion profile. (A) Remote sensing interpretation map around the microtremor survey line layout site near Xinxing; (B) Remote sensing interpretation map around the microtremor survey line layout site near East Xinxing; (C) Remote sensing interpretation map around the microtremor survey line layout site near Hongxing; (D) Shear-wave velocity inversion profile from microtremor survey line MTS-a; (E) Shear-wave velocity inversion profile from microtremor survey line MTS-b; (F) Shear-wave velocity inversion profile from microtremor survey line MTS-c.

signals from the array records were calculated using the SPAC method, and Rayleigh wave dispersion curves were extracted via frequency-Bessel function fitting. Finally, the dispersion curve was inverted using a genetic algorithm to

**Table 1. Micro-movement measurement line status report**

| Line number | Line length (m) | Point spacing (m) | Pile number (m) | Dip direction | Dip (°) | Fracture zone width (m) |
|---|---|---|---|---|---|---|
| MTS-a | 1600 | 10 | 600–700 | N | 60–70 | 60–100 |
| MTS-b | 1000 | 10 | 720–880 | N | 60–70 | 60–100 |
| MTS-c | 1000 | 10 | 200–300 | N | 60–70 | 60–100 |

obtain high-resolution shallow shear wave velocity (Vs) profiles for the study area. Shear wave velocity effectively reflects the compaction and diagenetic degree of strata. Generally, when Vs values are less than 500 m/s, strata are predominantly Quaternary loose sediments; when Vs exceeds 500 m/s, the strata can be identified as bedrock or strongly consolidated bedrock layers.

The results from the three survey lines (Table 1) indicate that all microtremor profiles exhibit a shallow low-velocity zone with Vs < 500 m/s in the upper part of the profile, representing debris flow deposits or fluvial/aeolian accumulation layers. Beneath this lies a bedrock layer with Vs > 500 m/s, separated by a distinct interface, indicating stable stratigraphic structure (Figure 7). In addition, some areas exhibit intermediate-velocity layers with Vs values between 500 and 800 m/s, approximately 70–80 m thick. These are interpreted as zones of fully weathered to strongly weathered bedrock. This layer appears as a transitional distribution in the microtremor profiles and serves as a key basis for fault identification and stratigraphic segmentation.

By comparing microtremor inversion results with field topographic phenomena, it was found that the profile structure exhibits a strong correlation with topographic features, such as variations in landslide deposit thickness and undulating elevations, as observed during field surveys. This suggests that microtremor profiles are highly reliable for identifying shallow geological structures.[36,37] Microtremor detection provides the 3D orientation and profile characteristics of deeper fracture sections. However, no significant anomalies in shear wave velocity were detected within the approximately 80 m thickness near the surface. Consequently, the near-surface structure and orientation of the fracture remain unclear. To more accurately reveal the fault's near-surface location and orientation, verification through trenching methods is required.

### 3.3. Validation by trenching

Test pits were excavated at the surface projections of anomalous zones identified in microtremor inversion profiles to reveal the location and orientation of faults near the surface and to verify the reliability of microtremor detection results. These are designated as Test Pits TC1, TC2, and TC3 (Figures 8-10). The phenomena exposed along these three profiles were similar. The main strata consisted of landslide debris characterized by relatively large gravel particles, poor rounding and sorting, and minor intercalations of fine-grained aeolian sediments. Stratification was indistinct.

#### *3.3.1. Trench TC1*

Trench TC1 is located approximately 600–700 m along the MST-a microtremor profile and is situated within a distinct linear fault zone (Figure 7A). The TC1 trench is approximately 40 m long and has exposed a complete Quaternary stratigraphic section.

The trench exposed two north-dipping reverse faults trending north with an inclination of approximately 40°, exhibiting an overall stepped distribution. The faults primarily manifest as granite bedrock thrusting over gravel layers, forming distinct fault scarps. The gravel layers can be subdivided into three zones: The northern fault is overlain by the uppermost gravel layer, and the southern fault is covered by the two layers of gravel above it (Figure 7A and B). This indicates that faulting activity occurred before the overlying strata were deposited.

Detailed photographs of the section (Figure 8C) and corresponding sketches (Figure 8D) clearly show that the fault cuts through from the reddish-brown basal layer to the light grey layer. A debris zone is visible around the fault plane, with some sedimentary layers showing signs of bending and compression deformation. The detailed cross-section on the opposite side (Figure 8E) and the corresponding sketch (Figure 8F) reveal multiple secondary faults. These faults predominantly penetrate upwards through the central gravel layer, with some exhibiting thrust-overlapping relationships. This indicates multi-phase faulting activity in this area.

#### *3.3.2. Trench TC2*

TC2 is located at the anomaly point along the micro-motion survey line MTS-B (Figure 7B). The trench excavation site is located at the bottom of an eroded gully characterized by significant topographical undulations. A thin layer of landslide debris covers the surface, and the exposed stratum comprises coarse-grained alluvial gravel deposits. Due to the loose strata and large gravel grain

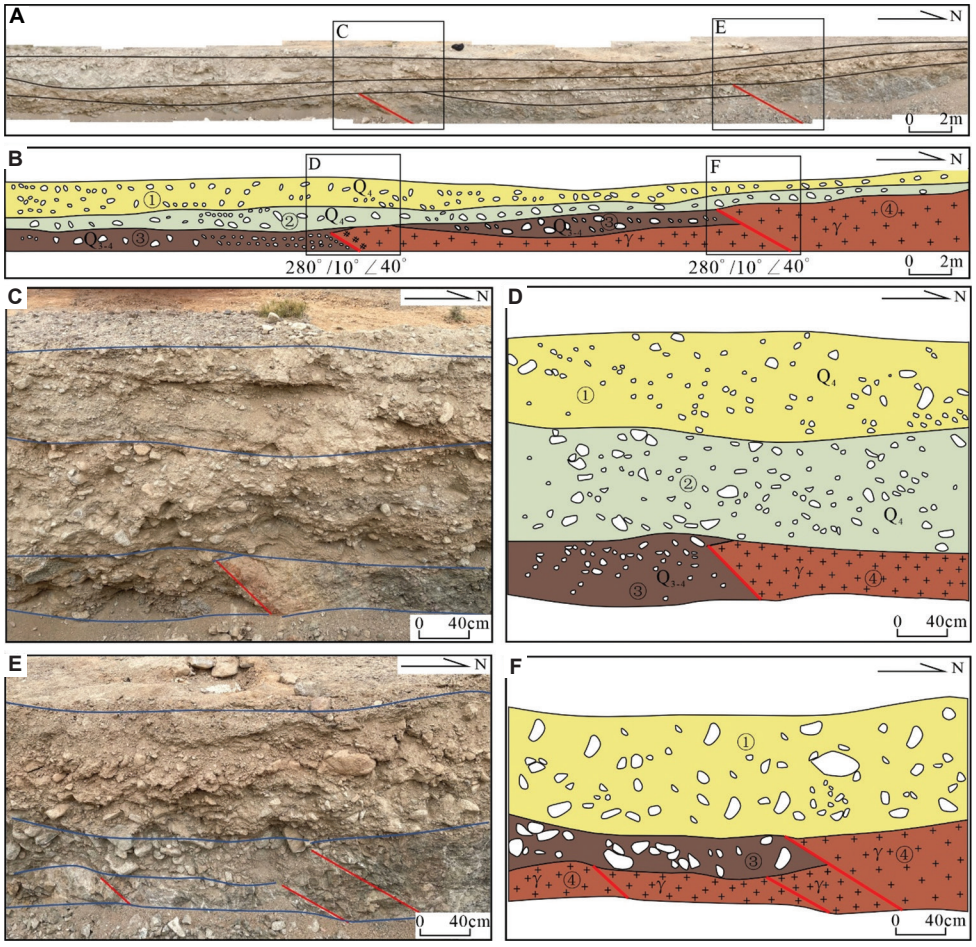


**Figure 8.** Analysis diagram of trench TC1. (A) Spliced photo of the trench; (B) Sketch profile of the trench; (C, E) Detailed photo of the trench; (D, F). Partial sketch of the trench.
Notes: (1) Light yellow slope-wash and proluvial gravel layer; (2) Gray-green alluvial-proluvial gravel layer; (3) Gray-brown gravel layer; (4) Granite.

size, excavation was challenging and resulted in uneven trench walls (Figure 9A). As can be seen from the trench profile (Figure 9A and C), the strata are mainly made up of Quaternary fluvial-colluvial gravels that exhibit the typical characteristics of alluvial fan deposition. Three stratigraphic units can be discerned from base to summit: a yellowish-grey layer containing boulders and gravel; a gray gravel layer; and a gray layer containing boulders and fluvial-colluvial gravel. The coarse gravel layer exhibits poor sorting and pronounced particle support, with localized large boulder flotation observed. The overlying gray, boulder-bearing fluvial-alluvial gravel layer is dominated by boulders, with indistinct bedding and localized blocky structures visible.

As shown in Figure 9B, an active fault structure was identified in the central section of the trench profile. The fault plane exhibits an overall southward dip with an inclination of approximately 45°. The fault cuts through the underlying coarse gravel layer and extends into the middle-upper strata. Sediments near the fault zone display pronounced structural deformation characteristics. Sediments on the hanging wall of the fault exhibit relatively coarse grain sizes and show signs of rearrangement. Within the shear zone, fine-grained material has been compressed, and local gravel has been reoriented along the fault plane to form elongated, banded structures. These structural bands indicate the direction of shear. Based on a combined assessment of the geometric structure of the fault and its tectonic characteristics, it is determined that this fracture is an active fault with pronounced thrusting characteristics.

The local sketch of the trench (Figure 9C) reveals that multiple small secondary slip surfaces have developed within the shear zone. These surfaces are interbedded with lenses of fine-grained sediments and clastic gravel. They are wedge-shaped, filling the interior of the fault, and their formation is suggested to have occurred through the superposition of multiple episodes of activity. Near the trench floor, the gravel layer is distinctly oriented at

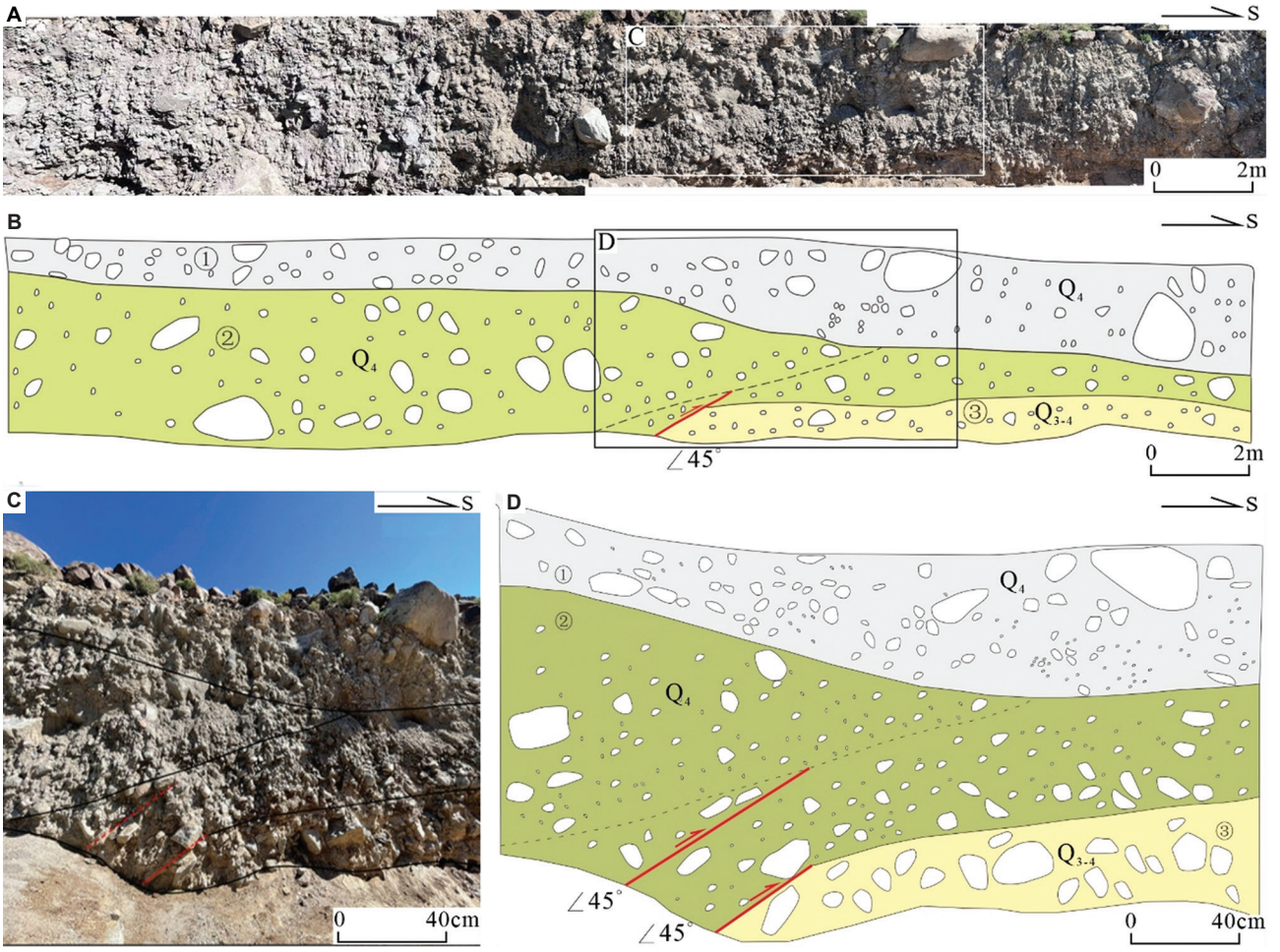


**Figure 9.** Analysis diagram of trench TC2. (A) Spliced photo of the trench; (B) Sketch profile of the trench; (C) Detailed photo of the trench; (D) Partial sketch of the trench.
Notes: (1) Gray diluvial-proluvial gravel layer with megaclasts; (2) Gray sandy gravel layer; (3) Yellowish-gray sandy gravel layer with megaclasts.

an angle to the original bedding. This indicates the fault's path, with an approximate dip angle of 45°.

The local sketch of the trench (Figure 9C) reveals that multiple small secondary slip surfaces have developed within the shear zone. These surfaces are interbedded with lenses of fine-grained sediments and clastic gravel. They are wedge-shaped, filling the interior of the fault, and their formation is suggested to have occurred through the superposition of multiple episodes of activity. Near the trench floor, the gravel layer is distinctly oriented at an angle to the original bedding. This indicates the fault's path, with a dip angle of approximately 45°.

Moreover, as can be seen from the cross-section and photographs, this fault primarily displaces the gravel layer deposited on the slope during the Q3 period. Due to the disordered deposition of this gravel layer, no dislocation is observed in the overlying layer, which is approximately 1 to 2 m thick.

### *3.3.3. Trench TC3*

Trench TC3 is located at the anomaly point identified along the MST-E profile (Figure 7C). The trench is located within a thin layer of debris flow deposits that cover the foothills, where the terrain is steeply sloped. The northern section of the trench exposed granite bedrock, while the southern section comprised coarse-grained debris flow deposits and fluvial-alluvial sediments with smaller gravel particles on the surface. Due to the thick, loosely structured overburden, excavation was challenging and resulted in uneven trench walls.

The strata exposed within the trench consist primarily of loose Quaternary deposits and heavily weathered granite. The southern section predominantly features Quaternary fluvial-alluvial deposits and landslide debris, while the northern section comprises heavily weathered granite bedrock overlaid by a layer of Quaternary landslide gravel. The central section of the trench lies within a concentrated

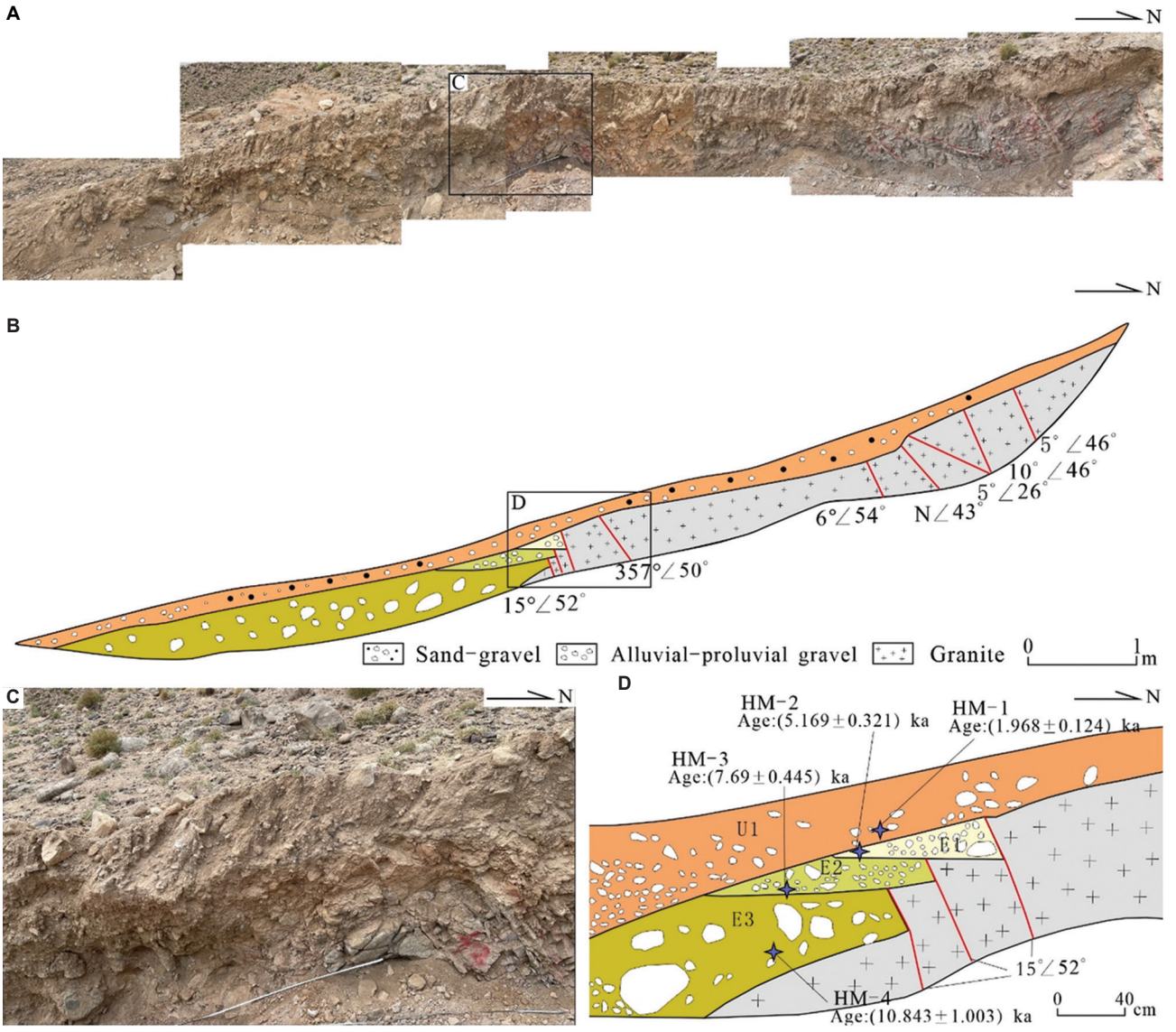


**Figure 10.** Analysis diagram of trench TC3. (A) Spliced photo of the trench; (B) Sketch profile of the trench; (C) Detailed photo of the trench; (D) Partial sketch of the trench.

fault zone where a distinct, stepped fault scarp is formed between the Quaternary deposits and the underlying bedrock (Figure 10C).

Multiple sets of faults developed within the northern section of the granite. These were primarily distributed along the contact zone between the Quaternary sediments and the granite, as well as within the overlying strata. The faults have a strike range of between 357° and 15° and a dip angle predominantly concentrated between 45° and 55°, though exceeding 50° locally in some instances (Figure 10A and B).

An active fault zone inclined from north to south was identified at the mid-section of the trench. This fault zone comprises three smaller sections (Figure 10D), designated as F1, F2, and F3. The fault zone cuts through both the granite bedrock and the overlying Quaternary gravel layer, creating a distinct, multi-tiered, step-like thrust structure. The parallel-to-strike foliation that developed along the sections indicates pronounced shear deformation characteristics.

Two wedge-shaped depositional sequences, controlled by fractures, formed in the central section of the trench. These sequences exhibit relatively consistent lithological characteristics. The basal layer consists of slightly bedded gravel containing moderately sorted, poorly rounded cobbles that predominantly exhibit angular morphology.

The upper section comprises an unbedded deposit of mixed gravel and silt clasts that lacks distinct bedding. This deposit was likely formed through rapid deposition or landslide processes. The lowest stratum also comprises a gravel layer deposited by a landslide containing boulders. Its contact surface with the underlying granite dips southwards, exhibiting localized shear-pull deformation (Figure 10D).

Based on the structural analysis of the cross-section, the magnitude of the vertical displacement of each fault varies. F1 exhibits the greatest displacement, at around 40 cm, while F2 and F3 show displacements of approximately 20 cm (Figure 10D). Furthermore, certain sections of the sedimentary layers show signs of traction deformation, such as bending and distortion. This indicates that fault activity caused displacement along the fault planes and was also accompanied by significant disturbance to the sediments. When this deformation is factored in, the cumulative vertical displacement of the fault system in trench TC3 could reach 1 m, revealing pronounced tectonic activity in the region since the Late Quaternary period.

In addition, optically stimulated luminescence dating samples were collected from this trench. Four sampling points were selected at the base of four marker layers, yielding a total of four samples to determine the depositional ages of each layer (Figure 10D). Testing revealed that some samples exhibited weak luminescence signals. Test results indicate that the luminescence ages for Layer U1 are 1.986 ± 0.124 ka, while those for Layers E1, E2, and E3 were 10.843 ± 1.003 ka, 7.69 ± 0.445 ka, and 5169 ± 321 ka, respectively (Table 2). This indicates that the fault has been active since the Holocene epoch.

## 4. Analysis and discussion

### 4.1. Geometric analysis of the fault plane

Based on remote sensing interpretation and field geological surveys, this study has determined the planar characteristics of this fault segment with considerable precision. Extending westward from the Miaogou area, the fault primarily runs along the southern foothills of the Halike Mountains, where they meet the Hami Basin. It then runs eastward through Hongxing Gou, to the east of the Bamudun River. The fault has a total length of approximately 35 km and strikes nearly east-west.

This fault segment is clearly visible as a linear feature in the satellite image and is manifested topographically as steep, discontinuous escarpments on the alluvial fan at the foot of the mountains. On the alluvial fan to the west of Miaogou, the fault markers are highly visible, with distinct escarpment landforms. The primary topographic manifestation comprises well-defined fault scarps that have formed on the T3 terrace and the alluvial fan that formed during the Late Pleistocene era. The escarpments generally reach heights of 12 m. Measurements of the fault scarp on the alluvial fan produced a profile showing a total height of 11 m (Figure 5F). Clear scarp features are also present on the river terrace along the eastern bank of the Bamudun River at its outlet, reaching a total height of 13 m (Figure 4F). Since the mid-Late Pleistocene, the primary geomorphological expression of this fault has been the presence of distinct scarps on the T3 terrace and the Late Pleistocene alluvial fan. These scarps exhibit a total height ranging from 11 to 13 m.

### 4.2. Fault geometry at depth

This study systematically analyzed the profile characteristics of the eastern segment of the northern margin fault in the Hami Basin by cross-verifying microtremor detection and trench profiles. The primary exposure zone of this eastern segment is the Miaoergou-Bamudun area, which generally trends in an east-west direction and exhibits the characteristics of a north-dipping reverse fault.

Microtremor survey method provides an excellent level of spatial detail for identifying faults, effectively capturing anomalous shear wave velocity distributions within fault zones in order to determine the locations and geometric parameters of faults preliminarily. In this study, three microtremor survey lines were deployed in combination with trench verification to systematically reveal key information, including precise fault locations, 3D orientation, and fracture zone width.

The microtremor profile along the MTS-a survey line indicates a zone of low velocity with an inclination of approximately 60°–70° between surface stations 600

**Table 2. The dating results of OSL samples from trench TC3**

| Sample ID | Test minerals | U (ppm) | Th (ppm) | K (ppm) | Moisture content (%) | Burial depth (m) | Environmental dose (Gy/ka) | Equivalent dose (Gy) | Age (ka) |
|---|---|---|---|---|---|---|---|---|---|
| HM-1 | Quartz | 6.79362 | 17.0734 | 2.41 | 0.427 | 0.3 | 6.99±0.417 | 13.756±0.283 | 1.968±0.124 |
| HM-2 | Quartz | 6.60067 | 19.25079 | 2.7467 | 0.0107 | 0.5 | 7.573±0.429 | 39.142±0.991 | 5.169±0.321 |
| HM-3 | Quartz | 6.1721 | 20.69530 | 2.57 | 0.0067 | 0.8 | 7.358±0.407 | 56.586±0.970 | 7.69±0.445 |
| HM-4 | Quartz | 6.4861 | 13.09402 | 1.60913 | 0.597 | 1.3 | 5.615±0.37 | 60.880±3.950 | 10.843±1.003 |

and 700 m. This zone is interpreted as fractured, with an estimated width of 60–70 m. At the corresponding location, trench TC1 exposed two northward-trending faults with an inclination of approximately 40°. These faults exhibit stepped displacement characteristics, with granite thrusting onto the gravel layer and clearly defined fracture structural features.

The microtremor profile along the MTS-b transect reveals a distinct low-velocity anomaly zone between surface stations 720 and 880 m. This zone exhibits an inclination of approximately 70°, with localized undulations at the surface. Trench TC2 revealed an oriented structure at the base of the gravel layer in this section that forms an angle with the original bedding. This is interpreted as a fault zone with an inclination of around 45°, exhibiting the characteristic geometry of a "steep at depth, gentle at shallower levels" fault.

The microtremor profile along the MTS-c survey line shows a zone of low-velocity anomalies with an inclination of around 60° between surface station numbers 200 and 300 m. This zone is around 100 m wide. Trench TC3 at the corresponding profile location revealed multiple north-dipping faults within the granite. These faults strike in an east-west direction and have dip angles ranging from 35° to 60°, which indicates intense tectonic disturbance.

Overall, geophysical surveys indicate fault dip angles of 60°–70°, whereas trenching has revealed shallower faults with comparatively gentler angles of dip of around 35°–60°. Integrating these findings suggests that the actual fault dip likely ranges between 35° and 70°. The fractured zone revealed by geophysical surveys may extend beyond the boundary fault to encompass areas with reduced strength. Analysis indicates that the width of the fractured zone ranges between 60 and 100 m.

### 4.3. Application of microtremor survey technology in active fault detection

Active fault detection serves as a vital technical approach for earthquake disaster risk prevention, major project site selection, and regional geological stability assessment.[38] At present, this field has established an integrated research system combining geological and topographical surveys with multi-source geophysical detection. Within this framework, geophysical detection plays a crucial role in the detailed identification of deep structures and the spatial localization of faults. In recent years, microtremor detection, as a passive-source geophysical method, has gained increasing application in active fault detection due to its advantages, such as strong resistance to interference and insensitivity to low-resistance layers. Compared to traditional geophysical methods like transient electromagnetic and resistivity surveys, microtremor detection is less susceptible to electromagnetic interference, high-low velocity interlayers, and low-resistivity shielding effects. It is particularly suitable for complex geological cover zones such as landslide deposits and coarse-grained alluvial deposits, effectively identifying geotechnical structural variations and delineating fault fracture zones.[39,40]

This study investigates the Shangmiyang–Bamudun segment of the eastern section of the northern margin fault in the Hami Basin, employing microtremor detection technology to explore deep geological anomalies. Based on array data collected along three survey lines, a shear wave velocity profile was inverted. Results show that the profile clearly distinguishes Quaternary loose deposits from underlying bedrock: Layers with shear wave velocities below 500 m/s are identified as Quaternary loose sediments, while those above 500 m/s correspond to bedrock. Within the inverted profile, slope-deposited materials with velocities below 500 m/s overlie the bedrock, consistent with the geological and topographic characteristics of the area (Figure 6). Furthermore, the profile reveals a stratum with velocities below 800 m/s has a thickness of approximately 80 m, interpreted as a layer of fully weathered to strongly weathered bedrock.

All three microtremor profiles reveal a low-velocity anomaly zone, with shear wave velocity isopleths exhibiting a banded or elongated elliptical distribution. The major axis trends northward at an inclination of approximately 60°, interpreted as a typical response of a fault breccia zone. Active fault fracture zones typically feature loose rock masses with low strength, creating anomalies characterized by relatively low wave velocities. This anomaly zone aligns with the location of a steep surface scarp, further supporting the interpretation as a fault fracture zone. Microtremor detection effectively revealed the 3D orientation and profile characteristics of the deep fracture zone. However, within approximately 80 m near the surface, the lack of significant anomalies in stratigraphic wave velocity made it difficult to identify shallow fracture structures and orientations, highlighting the method's limitations in shallow detection. Nevertheless, microtremor detection remains a valuable technical tool for fracture identification and 3D structural imaging.

## 5. Conclusion

This study is based on remote sensing interpretation and geological-morphological surveys, and prioritizes the incorporation of microtremor detection technology. Through integrated analysis and cross-validation using multiple methodologies, including drilling and trenching,

the study precisely delineates the spatial distribution and 3D characteristics of the eastern segment of the northern margin fault in the Hami Basin. The results show that microtremor detection has excellent resolution capabilities in foothill areas with thin overburden or coarse gravel. This provides effective technical support for identifying active faults in complex terrain.

The eastern segment of the northern margin fault of the Hami Basin runs along the southern foothills of the Halik Mountains. It extends in a nearly east-west direction from Miaogou to the Bamudun River area. This fault is clearly visible as distinct linear features in high-resolution remote sensing image and is manifested topographically as steep, discontinuous scarps on the alluvial fan at the foot of the mountains. This reflects tectonic activity dominated by thrust deformation since the Quaternary period. Field surveys indicate typical steep scar heights of up to 11 m. Fault traces are clearly discernible on the river terrace along the eastern bank of the Bamudun River outlet, demonstrating significant activity.

The results of the microtremor detection indicate that the fault zone within the study area is approximately 40 m wide, with the most extensively fractured zone reaching up to 100 m in width. The fault's overall dip angle is approximately 60°. Drilling and trenching within the high velocity zone revealed multiple fault planes, all of which dip northwards at a shallow angle of approximately 45°. This aligns well with the structural anomalies exposed by the microtremor profile. The fault exhibits a distinct "steep at depth, gentle near surface" geometric pattern, indicating a steep dip at greater depths that gradually flattens toward the near-surface zone.

In summary, microtremor detection technology has proven highly adaptable and practical for identifying active faults in this region. It has been shown to be effective in areas with complex topography and thick overburden. This study pinpoints the precise location and geometric morphology of the eastern segment of the northern margin fault in the Hami Basin, providing crucial reference data for regional seismic hazard assessment and major project site selection. Furthermore, it expands the potential applications of microtremor detection technology in active tectonic research, with significant theoretical implications and practical engineering value.

## Acknowledgments

We sincerely thank Senior Engineers Xiaodong He, Yanling Liu, Junqi Duan, Jun Ma, and other professionals from PowerChina Northwest Engineering Corporation Limited for providing geological and geophysical data as well as their assistance and guidance during fieldwork. Meanwhile, we also express our gratitude to Associate Professor Zhitao Gao, Qian Zhao (engineer), and Xuefeng Zhao (student) from the Institute of Disaster Prevention and Beijing Disaster Prevention Science and Technology Co., Ltd. for their contributions to the implementation of relevant projects.

## Funding

This research was supported by the National Natural Science Foundation of China (Grant No. 42172253) and received substantial support from the "Specialized Survey on Fault Distribution and Activity at the Northern Margin of the Hami Basin" project, which was jointly undertaken by China Power Engineering Consulting Group Northwest Survey and Design Institute Co., Ltd. and Beijing Disaster Prevention Science and Technology Corporation Limited.

## Conflict of interest

The authors declare no conflicts of interest.

## Author contributions

*Conceptualization:* Jun Shen, Guanghong Ju
*Formal analysis:* Jun Shen
*Funding acquisition:* Jun Shen
*Investigation:* Jun Shen, Xu Song, Guanghong Ju
*Methodology:* Jun Shen, Guanghong Ju
*Project administration:* Guanghong Ju
*Validation:* Jun Shen, Guanghong Ju
*Visualization:* Xu Song
*Writing–original draft:* Xu Song
*Writing–review & editing:* Jun Shen

## Availability of data

Data are available from the corresponding author on reasonable request.

## References

1. Xu XZ, Wang YX, Jiang YM, Jiang YM, Dang SJ, Nie DP. [Crustal velocity structure and geotectonic units division of the Xinjiang-Gansu seismic sounding profile]. *Xinjiang Geol.* 1992;10(2):147-154. [Article in Chinese].
2. Wu FY. [*Late quaternary Activity Evidence and Deformation Mechanism of Several Major Faults in the Eastern Section of the Eastern Tianshan Mountains*]. Beijing: Institute of Geology, China Earthquake Administration; 2016. [Article in Chinese].
3. Ren GX. [*Late Quaternary Activity and Tectonic Transformation of the Eastern Tianshan sinistral Strike-Slip Faults*]. Beijing: Institute of Geology, China Earthquake Administration; 2021. [Article in Chinese].
4. Bai MX, Luo FZ, Li J, *et al.* [Micro-geomorphology of the

active fault zone on the Northern Margin of Hami Basin]. *Inland Earthq.* 1999;13(2):162-168. [Article in Chinese]

5. Fang SM, Zhang XK, Liu BJ, Xu XW, Bai DH, JI JFl. [Geophysical methods for detecting active faults in large cities]. *Seismol Geol.* 2002;24(4):606-613. [Article in Chinese].
6. Wu JP. [Geophysical methods for urban seismic active fault detection]. *Seismol Geol.* 2000;22(1):1-15. [Article in Chinese].
7. Li QZ. [*The Road to Precision Prospecting: A Systematic Analysis of High-Resolution Seismic Exploration*]. Beijing: Petroleum Industry Press; 1993. p. 120-130. [Article in Chinese].
8. Lu JM, Wang YG, Dou H, He XH. *[Principles of Seismic Exploration*]. Beijing: Petroleum Industry Press; 1993. p. 140-156. [Article in Chinese].
9. Okada H. *The Microtremor Survey Method*, *Geophysical Monographs Series*. Vol. 12. Houston: Society of Exploration Geophysicists; 2003. p. 1-135.
10. Okada H. Theory of efficient array observations of microtremors with special reference to the SPAC method. *Explor Geophys*. 2006;37:73-85.

    doi: 10.1071/eg06073
11. Matsuoka T, Umezawa N, Makishima H. Chika kozo suiteino tame no kukan jiko sokanho no tekiyosei ni kansuru kento[Experimental studies on the applicability of the spatial autocorrelation method for estimation of geological structures using microtremors]. *Butsuri Tanko (Geophys Explor)*. 1996;49:26-41.
12. Cho I, Nakanishi I, Ling SQ, Okada H. Application of forking geneticalgorithm fga to an exploration method using microtremors. *Geophys Explor.* 1999;52:227-246.
13. Liu HP, Boore DM, Joyner WB. Comparison of phase ve-locities from array measurements of Rayleigh waves associated with mi-crotremor and results calculated from borehole shear-wave velocity pro-files. *Bull Seismol Soc Am.* 2000;90(3):666-678.
14. Zhao HP, He DK, Hong Y. Inversion of microtremor recordingsdispersion curve based on geological unit. *J Min Sci Technol.* 2022;7(6):662-669.

    doi: 10.19606/j.cnki.jmst.2022.06.003
15. Qiu P, Wang JH. [Application of microtremor and shallow seismic reflection technology in the detection of concealed sections of the Weining-Shuicheng fault structure]. *Guizhou Geol.* 2023;40(2):134-139. [Article in Chinese].
16. Feng SK. [Microtremor survey technology and its application in civil engineering]. *Chin J Rock Mech Eng.* 2003;22(6):1029-1036. [Article in Chinese].
17. Xu PF, Li SH, Ling SQ, Guo HL, Tian BQ. [Estimation of crustal S-wave velocity structure using the SPAC method]. *Chin J Geophys.* 2013;56(11):3846-3854. [Article in Chinese].
18. Xu PF, Li SH, Du JG, Ling SQ, Guo HL. :[Microtremor survey: A new method for stratigraphic division and concealed fault structure detection]. *Acta Petrol Sin*. 2013;29(5):1841-1845. [Article in Chinese].
19. Windley BF, Allen MB, Zhang C, Zhao ZY, Wang GR. Paleozoic accretion and Cenozoic redeformation of the Chinese Tien Shan Range, central Asia. *Geology*. 1990;18(2):128.

    doi: 10.1130/0091-7613(1990)018<0128:PAACRO>2.3.CO;2
20. Molnar P, Tapponnier P. Cenozoic tectonics of Asia: Effects of a continental collision. *Science*. 1975;189(4201):419-426.

    doi: 10.1126/science.189.4201.419
21. Avouac J P, Tapponnier P, Bai MX, You H, Wang G. Active thrusting and folding along the northeastern Tien Shan, and late Cenozonic rotation of the Tarim relative to Dzungaria and Kazakhstan. *J Geophys Res.* 1993;98(B4):6755-6804.
22. Hendrix MS, Dumitm TA, Graham SA. Late oligocene-early miocene unroofing in the Chinese Tianshan: An early effect of the India-Asia collision. *Geology*. 1994;22(6):487-490.

    doi: 10.1130/0091-7613(1994)022<0487:loemui>2.3.co;2
23. Deng QD, Feng XY, Zhang PZ, *et al*. [*Active Tectonics of the Tianshan Mountains*]. Beijing: Seismological Press; 2000. p. 7. [Article in Chinese].
24. Deng QD, Zhang PZ, Ran YK, Yang XP, Min W, Chu QZ. [Basic characteristics of active tectonics in China]. *Sci China Ser D Earth Sci.* 2002;45(12):1020-1030. [Article in Chinese].
25. Yang XP, Deng QD, Zhang PZ, Xu XW. [Crustal shortening in the major nappe structure zone of the Tianshan piedmont]. *Seismol Geol*. 2008;30(1):111-131. [Article in Chinese].
26. Zhang PZ, Deng QD, Zhang ZQ, Li HB. [Active faults, earthquake hazards and associated geodynamic processes in mainland China]. *Sci China Earth Sci.* 2013;56(10):1607-1620. [Article in Chinese].
27. Tapponnier P, Molnar P. Active faulting and tectonics in China. *J Geophys Res.* 1977;82(20):2905-2930.

    doi: 10.1029/JB082i020p02905
28. Tapponnier P, Molnar P. Active faulting and Cenozoic tectonics of the Tien Shan, Mongolia, and Baykal Regions. *J Geophys Res Solid Earth*. 1979;84(B7):3425-3459.

    doi: 10.1029/JB084iB07p03425
29. Zhang PZ, Deng QD, Yang XP, Peng SZ, Xu XW, Feng XXY. [Late Cenozoic tectonic deformation of the Tianshan Mountains and associated geodynamic processes]. *Earthq Res China*. 1996;12(2):127-140. [Article in Chinese].
30. Wu CY, Wu GD, Shen J, Dai XY, Song H. Late quaternary tectonic activity and crustal shortening rate of the Bogda Mountain Area, Eastern Tian Shan, China. *J Asian Earth Sci.* 2016;119:20-29.

doi: 10.1016/j.jseaes.2016.01.001

31. Huang ST, Hu WH, Yang PX, Li S, Yin LYE. [Late quaternary activity characteristics of the Tangbale-Tasidun Fault Zone in Eastern Tianshan]. *Seismol Geol.* 2020;42(5):1058-1071. [Article in Chinese].
32. Ma J, Chen JB, Zhao CQ, Liu ZJ. [Late quaternary activity characteristics of the Yiwu Fault in Eastern Tianshan Region]. *Inland Earthq.* 2021;35(1):87-92. [Article in Chinese].
33. Yang X, Wu CY, Li ZG, Wang W, Chen G, Duan L. Late quaternary kinematics and deformation rate of the huoyanshan structure derived from deformed river terraces in the South piedmont of the Eastern Chinese Tian Shan. *Front Earth Sci.* 2021;9(9):649011.

    doi: 10.3389/feart.2021.649011
34. Feng XY. [Study on holocene active faults and paleoearthquakes in Tianshan Mountains]. *Inland Earthq.* 1995;9(3):217-226. [Article in Chinese].
35. Li YZ, Shen J. [Seismic geology and seismicity in Hami Region, Xinjiang]. *Inland Earthq.* 2001;15(2):141-147. [Article in Chinese].
36. Shi K, Yang FQ, Li YF, Mo YJ, Qu XY. [Investigation of urban underground space structures using microtremor detection]. *Min Resour Geol.* 2020;34(2):355-365. [Article in Chinese].

    doi: 10.19856/j.cnki.issn.1001-5663.2020.02.024
37. Liu BY, Chen JH, Liu YQ, Zhao L, Sun YP. [Two-dimensional microtremor profiling at Linxia Airport, Gansu Province]. *Geod Geody.* 2023;43(12):1235-1239. [Article in Chinese].

    doi: 10.14075/j.jgg.2023.03.106
38. Deng QD, Lu ZX, Yang ZE. [Urban active fault detection and fault activity assessment]. *Seismol Geol.* 2007;29(2):189-200. [Article in Chinese].
39. Ding LF, Xu PF, Ling SQ, Zhao CJ, Li CJ. [Detection of magmatic rock intrusion in LinNanCang Coal Mine by microtremor exploration method]. *Coal Sci Technol.* 2010;38(7):100-103. [Article in Chinese].
40. Liu YQ, Liao YG, Li XZ, Pang W. [Application of microtremor survey technology in rail transit engineering investigation]. *J Geotechn Investig Surv.* 2010;Suppl 1:1-11. [Article in Chinese].